Phased Array Measurements of a Full-Scale Helicopter

Kyle A. Pascioni
Research Aerospace Engineer
NASA Langley Research Center
Hampton, VA, USA

Colin M. Stutz
Research Aerospace Engineer
NASA Langley Research Center
Hampton, VA, USA

Mary L. Houston
Research Aerospace Engineer
NASA Langley Research Center
Hampton, VA, USA

James H. Stephenson
Aviation Acoustics Subject Matter Expert
U.S. Army Combat Capabilities Development Command
Aviation & Missile Center
Hampton, VA, USA

ABSTRACT

Single microphone measurements lack the ability to separate nondeterministic noise sources on multipropulsor vehicles, limiting their usefulness to understand the dominant noise generation mechanisms. To advance the state-of-the-art for measuring multipropulsor aircraft in support of future Urban Air Mobility (UAM) and Future Vertical Lift (FVL) testing, a 117-channel phased array was deployed during an Army/NASA acoustic flight test of an MD530F helicopter. A time-domain beamforming algorithm, namely, the ROtating Source Identifier (ROSI), was utilized to track the aircraft's forward motion and main rotor rotation. This process isolates nondeterministic sources of the main rotor, effectively filtering out contributions of the tail rotor and other nonrotating components. Source maps are provided for low-speed forward flight and illustrate aeroacoustic sources near the main rotor blade tips over a broad frequency range. Particular emphasis is given on the benefits of flying at a lower altitude relative to the array to enhance source separation through increased spatial resolution. A coherence-based microphone weighting scheme was utilized to support component-based integrated spectral assessments. Total integrated levels over the rotating scan grid are provided, representing the contribution of the main rotor to the total aircraft levels. Although additional analysis is needed to gain confidence in the beamforming methods applied, results herein minimally indicate this to be a valuable technique for qualitative source ranking.

NOTATION

a_r	Rotor disk area (m^2)
A_h	Source strength within integration region at scan point h
$A_{s,h}$	Source strength of PSF within integration region at scan point h
C_W	$= W/(\rho_0 a_r(60\omega R)^2)$, weight coefficient
D	Estimated fuselage drag (N)
f	Frequency (Hz)
f_d	Effective flat plate drag area (m^2)
$\mathcal{F}(\cdot)$	Fourier transform
L_γ	Coherence length scale (m)
N	Number of microphones
P	Integrated source power (Pa^2/Hz)
P_s	Integrated source power of PSF (Pa^2/Hz)
PSF	Point spread function
r_j	Radial location of scan point j (m)
r_n	Radial location of microphone n (m)
R	Main rotor radius (m)
w	Microphone weighting
W	Vehicle weight (N)
(x_j, y_j, z_j)	Coordinates of scan point j (m)
(x_h, y_h, z_h)	Coordinates of main rotor hub (m)
z_c	Altitude correction term (m)
α_{TPP}	Tip path plane angle of attack (rad.)
γ	Flight path angle (deg.)
γ^2	Ordinary magnitude-squared coherence
λ^2	Associated aperture area of each microphone (m^2)
ω	Rotation rate (rev./s)
$\tilde{\sigma}$	Estimated source signals, per microphone (Pa)
σ	Reconstructed source signals (Pa)
θ_j	Initial angular location of scan point j (deg.)
ψ	Scan grid rotation phase angle (deg.)
ρ_0	Ambient density (kg/m^3)
τ	Source time (s)

INTRODUCTION

Acoustic measurements of full-scale conventional helicopters, Urban Air Mobility (UAM) aircraft, and Future Vertical Lift (FVL) concepts are often difficult to interpret and extract physical insight. Consider, for example, the resulting spectrum of the UH-1A helicopter in hover provided in Figure 1 (Ref. 1). Many spectral features are pointed out, with the responsible rotor or source mechanism identified. In this par-

Presented at the Vertical Flight Society's 81st Annual Forum & Technology Display, Virginia Beach, VA, USA, May 20–22, 2025.

ticular case, the main rotor broadband noise overlaps the frequency range of the tail rotor rotational noise, making it difficult to fully determine the relative contributions. These type of frequency domain results become increasingly more challenging to interpret for certain helicopter rotor configurations, and even more so for aircraft that employ distributed propulsion. Thus, it is useful to apply signal decomposition methods or advanced measurement techniques.

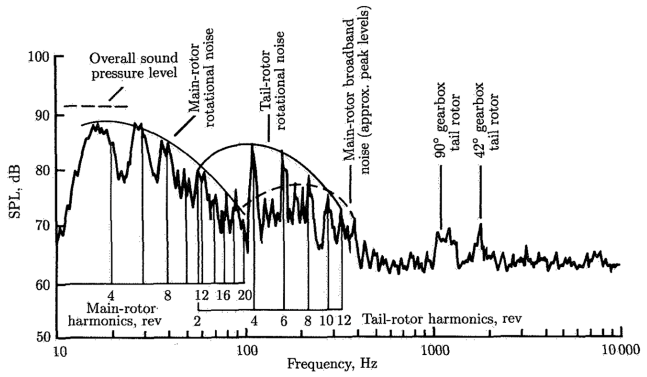

Figure 1. Example spectra of a UH-1A helicopter indicating the complex nature of full-scale measurements (Ref. 1).

Due to the rotating nature of the propulsors (e.g., rotors, propellers), deterministic and nondeterministic aeroacoustic content are generated. Deterministic sources include harmonic noise comprised of steady thickness, steady or periodic loading, and parallel blade-vortex interaction (BVI) noise. For these phenomena, phase averaging (Ref. 2) or wavelet-based decomposition methods (Ref. 3) applied to single-microphone measurements have enabled separation of acoustic information between the main and tail rotor of a conventional helicopter. More recently, order tracking methods have been applied to better separate harmonic content between two rotors (Ref. 4), as well as distributed propulsion systems with six propulsors on an Unmanned Aerial System (UAS) (Ref. 5) and a full-scale Vertical Take-Off and Landing (VTOL) platform (Ref. 6). A collection of microphones distributed over ground-based emission angles, e.g., a snapshot array (Refs. 7, 8), can be useful to characterize directivity of harmonic content, which can vary significantly over different operational conditions.

Nondeterministic sources (e.g., turbulence ingestion noise, rotor-wake interaction noise, airfoil self-noise) are expected to be important and potentially dominant for novel multi-propulsor vehicles; however, these phenomena are difficult to model (Ref. 9). The stochastic nature of these sources makes it challenging to identify what component(s) of the aircraft contribute to, and dominate, the total acoustic field. Thus, a method to measure these relative contributions and gain more physical insight into these noise generation mechanisms is desired.

Microphone phased arrays have offered a solution to identify dominant sources on a component level from flight test measurements of fixed-wing aircraft with great success (Refs. 10–12). Unlike snapshot arrays, phased arrays typically only characterize the source over a small directivity range. Fortunately, nondeterministic sources, often the result of unsteady aerodynamic loading, will behave as dipole sources with maximum directivity normal to the surfaces responsible for producing the noise. Thus, for takeoff and landing of conventional rotorcraft and many UAM configurations, i.e., those with tilting or dedicated lifting propulsors, such noise sources are expected to dominate below the aircraft. Directivity aside, the frequency spectrum peaks at mid- to high-frequencies, where atmospheric attenuation has a greater effect, further reducing ground levels (hence, importance) at other emission angles.

Beamforming techniques applied to rotating sources have been more limited than their application to stationary aircraft components, although several efforts have proven their validity for source noise decomposition on wind turbines, helicopter rotor wind tunnel tests (Refs. 13–15), and a ground-based static propeller test (Ref. 16). The latter demonstrated increased accuracy of source levels using rotational beamforming algorithms when compared to conventional methods. Although not investigated herein, it should be noted that wavelet-based beamforming methods also show promise for rotating sources by incorporating the Doppler effect and producing acoustic images in the time-frequency domain (Refs. 17, 18).

Building upon those efforts, the current effort is unique in that rotating beamforming algorithms will be applied to recent full-scale flight test measurements involving both forward and rotating motion. The data were recently acquired on a civilian helicopter from a joint U.S. Army/NASA acoustic flight test (Ref. 7). Additionally, this work will emphasize the source separation capabilities between two rotors (a main and tail rotor in this case), to better anticipate and plan for future UAM tests that may involve a high number of propulsors.

AIRCRAFT DESCRIPTION

The test aircraft was an MD530F, as configured in Figure 2, which is a light-utility civilian helicopter with a single 650 HP Rolls-Royce 250-C30 turboshaft engine; additional characteristics are provided in Ref. 7. Aircraft positional and inertial state data were recorded with NASA's second generation Aircraft Navigation and Tracking System (ANTS2) (Ref. 19). Tachometer data from the main rotor are also available and will be used for processing. All aircraft state data were synchronized with the acoustic measurements using Universal Coordinated Time (UTC).

FLIGHT CONDITIONS

Flight conditions over the phased array involved constant true airspeed level flyovers from 20 to 110 kt at 30 and 60 m above ground level (AGL), descents between 40 and 110 kt with flight path angles at -1.5°, -3°, and -6°, and shallow (2°-3°) ascents at 60 and 75 kt. One or more repeats were captured for each condition totaling approximately 50 test points. Additionally, hovers were performed at three different heights to

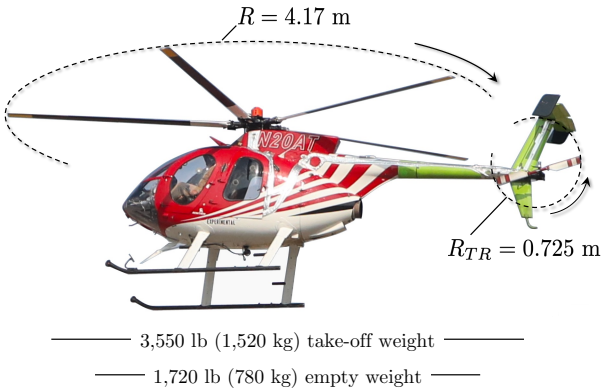

Figure 2. The MD530F helicopter, annotated with rotor radii.

study source map spatial resolution differences, with a minimum of 60 m altitude above ground level (AGL) to avoid excessive downwash and flow noise on the microphones. Many conditions overlap with those flown over the snapshot array, which was intended to capture acoustic levels at all emission angles (Ref. 8). To initialize this phased array flight test investigation on rotating sources, the results will focus on low speed forward flight at 20 kt true airspeed at both 30 and 60 m AGL.

GROUND-BASED INSTRUMENTATION

Phased Array Design

The phased array consisted of 117 microphones deployed on an extended concrete pad adjacent to a runway. Two geometries were deployed during the flight test. The first utilized a 40 m diameter layout and was a nested design consisting of a 45-element inner array and a 72-element outer array to enable a broad working frequency range. Both subarrays were the result of an optimization to minimize the 3 dB beamwidth while maintaining peak sidelobes 10 dB down from the main lobe and constrained channel count. The aperture was selected to provide reasonable spatial resolution relative to the helicopter main rotor geometry as viewed from a 60 m working distance.

Although spatial resolution based on the point spread function was commensurate with source separation requirements relative to the aircraft geometry, initial investigation proved that the microphone spacing was too large to capture enough coherence to provide accurate level estimates at the higher frequencies of interest. The cause of this is likely decorrelation of the acoustic wavefronts as they propagate, due to atmospheric turbulence (although wind conditions were very benign) or propagation through the wake of the main rotor. Alternatively, directivity nonuniformity over the array face could have also played a role.

To increase suitability for higher frequencies, the array aperture was scaled down to 12 m for the second flight day (referred to as FLT 209 in Ref. 7). The array pattern remained unchanged otherwise. Figure 3 displays this modified array as it was deployed, which will be the focus of this paper. Although spatial resolution will be lower than the original design, advanced beamforming techniques may be used in the future to reduce the effect of the array response to better depict the source field.

Data Acquisition

Two systems were used to record the microphone signals, both at 50 kHz with 24-bit resolution. The outer array was sampled using the second-generation Wireless Acoustic Measurement System (WAMS II), the primary acoustic flight test system for NASA rotorcraft and UAM research (Refs. 19, 20). Each station of this remotely controlled system consists of a 1/2-inch (12.7 mm) GRAS 67AX microphone embedded in a 400 mm diameter round ground board, a radio antenna, GPS receiver, and an on-board SD card for data recording.

The secondary data acquisition system acquired signals from the inner array, using an NI PXIe-1085 chassis with three NI PXIe-4499 data acquisition cards, each with 16 channels controlled via a local desktop. This system simultaneously sampled 45 Knowles WP-23849 microphones, each modified with a custom two-wire, low-noise, 4 mA constant current excitation system (Ref. 12). GPS timing was acquired using an NI PXI-6683H card with associated antenna enabling synchronization with the WAMS II data.

Weather

Wind speed and direction adjacent to the phased array were recorded during each test point at eight altitudes up to 60 m using a ZephIR 300 LiDAR vertical wind profiler. Ground temperature at the array was recorded and will be used to estimate the sound speed. A temperature string attached to a weather balloon gathered vertical profiles during the acoustic acquisition and can be used for future studies.

METHODS

The ROtating Source Identifier (ROSI) by Sijtsma (Ref. 13) is a time-domain beamforming algorithm that will be implemented herein. This procedure attempts to track and localize noise sources on rotating components using a stationary microphone phased array.

The coordinate system origin is defined at the center of the $N-$channel phased array, in which $+x$ is along the North-bound flight direction, $+y$ is to the port side of the aircraft, and $+z$ is up (see Figure 4). The microphone coordinates are known to centimeter accuracy upon measuring their positions using a differential GPS survey system. A scan grid is defined in the plane of the main rotor and rotates at the same rate. The center of rotation tracks the main rotor hub (x_h, y_h, z_h), accounting for the aircraft's translational motion in forward flight. The data used will be limited to ± 25 m relative to the array center, to avoid large phased array viewing angles that typically distort the source maps. At a 20 kt forward flight airspeed, approximately 40 main rotor revolutions will be used.

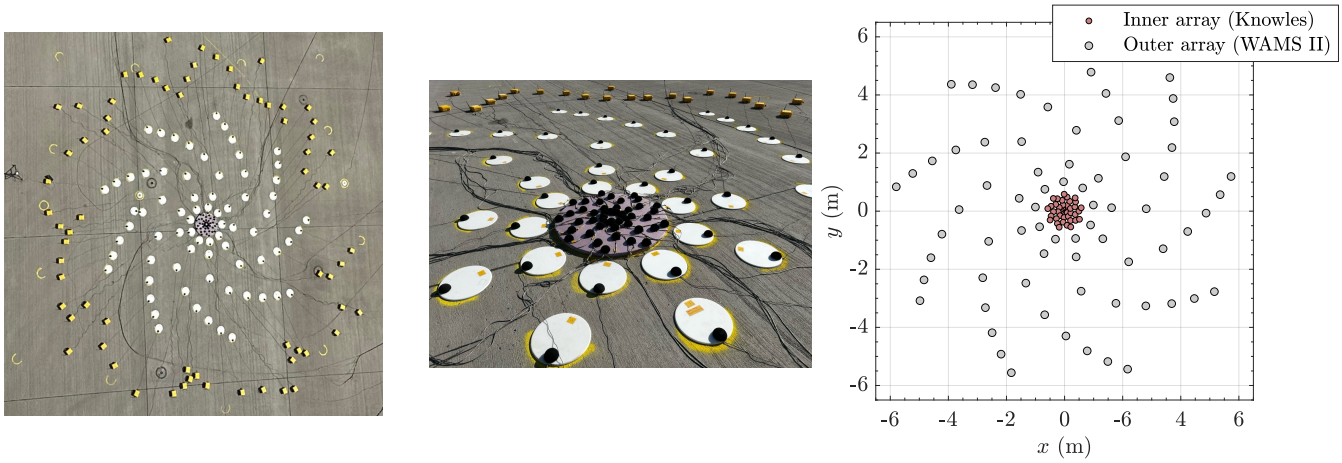

Figure 3. Phased array as viewed from the helicopter (left), on the ground (middle), and with microphone coordinates.

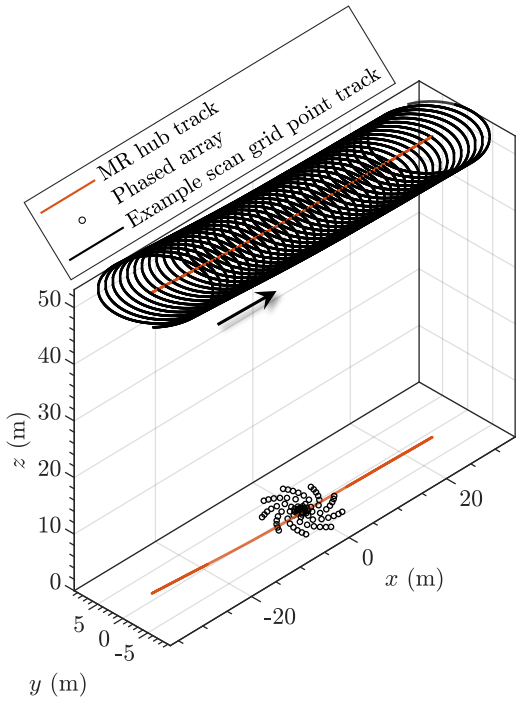

Figure 4. Flight path and phased array with an example of scan grid tracking of the main rotor.

The time-varying position of the jth scan grid point at r distance away from the center of rotation and at initial angle θ,

$$r_j = (x_j^2 + y_j^2)^{1/2}, \tag{1}$$

$$\theta_j = \tan^{-1}\left(\frac{y_j}{x_j}\right), \tag{2}$$

can be defined in three dimensions as

$$x_j(\tau) = x_h + r_j \cos(-\alpha_{TPP}) \cos\left(\psi(\tau) + \theta_j\right), \tag{3}$$

$$y_j(\tau) = y_h + r_j \sin\left(\psi(\tau) + \theta_j\right), \tag{4}$$

$$z_j(\tau) = z_h + r_j \sin(-\alpha_{TPP}) \cos\left(\psi(\tau) + \theta_j\right) + z_c. \tag{5}$$

For nonaccelerating flight, the tip path plane angle of attack, α_{TPP} (negative refers to the rotor disk tilting forward), is used to align the scan grid with the main rotor plane and can be approximated to first-order (Ref. 21),

$$\alpha_{TPP} = -\frac{D}{W} - \gamma, \tag{6}$$

in which D is the fuselage drag, W is the vehicle weight, and γ is the flight path angle (negative refers to a descent). The drag-to-weight ratio was estimated using the equation below,

$$\frac{D}{W} \approx \frac{f_d}{a_r} \frac{\mu^2}{2C_W} \tag{7}$$

in which $C_W = W/(\rho_0 a_r (2\pi\omega R)^2)$ is the weight coefficient, ρ_0 is the ambient density, a_r is the rotor disk area, ω is the average main rotor rotation rate (with units rev/s) over the flyover event, and R is the main rotor radius. Following the method by Ref. 22, a functional fit of the form,

$$\theta = -\frac{f_d}{2C_W a_r}\mu^2 + \theta_s, \tag{8}$$

was used to estimate the relationship between the measured vehicle pitch (θ) versus advance ratio (μ) over all level flight speeds tested. The curve fit enabled the effective flat plate drag of the fuseage, f_d/a_r, and the main rotor shaft pitch angle (mast tilt), θ_s, to be determined, yielding the appropriate inputs to equation 7 and subsequently equation 6.

Ideally, helicopters have constant rotor rotation rates. Investigation of the measured rates shows variations on the order of a few percent. To avoid smearing the source maps, the measured time-varying rotation rate is used to determine the associated scan grid rotation angle at source time τ,

$$\psi(\tau) = 2\pi \int_0^\tau \omega(u)\mathrm{d}u. \tag{9}$$

The last thing to note regarding the definition of the scan grid is the altitude correction term, z_c, in equation 5. Initial assessments of the source locations, particularly those at the blade

tips, were found to be incorrectly positioned outside of the rotor disk. It was determined this was due to uncertainty in the altitude tracking data, the component that typically has the largest error when using GPS-based tracking. Therefore, this correction was applied, and is of $\mathcal{O}(1)$ m.

With the microphone coordinates and time-varying position of the scan grid defined, the next step is to transform the measured acoustic signals to source signals, e.g., $p_n(t) \rightarrow \tilde{\sigma}_{j,n}(\tau)$. This transformation should be performed for each microphone and scan grid point pair. To achieve this, a time-domain de-Dopplerization technique is applied (Ref. 2), which involves an interpolation process effectively reducing the source signal sampling rate to 40 kHz. Note that for the two-dimensional grid ± 6 m in size with 0.1 m resolution used here, this transformation needs to be computed approximately 1.7×10^6 times. Thus, care should be taken when defining grid resolution. For this work, a 20-core CPU was run in parallel to expedite this step.

With the source signals in hand, the time-domain delay and sum method to estimate the source signal for point j in the scan grid is simply

$$\sigma_j(\tau) = \frac{1}{N} \sum_{n=1}^{N} \tilde{\sigma}_{j,n}(\tau). \tag{10}$$

However, a Fourier transform is preferred to enable frequency-dependent source maps to be visualized. Following the formulations presented by Ref. 13, the source strength at each scan point for the kth frequency bin becomes

$$A_{j,k} = \frac{1}{2N^2} \sum_{n=1}^{N} \sum_{m=1}^{N} \mathcal{F}_k(\tilde{\sigma}_{j,n}) \mathcal{F}_k(\tilde{\sigma}_{j,m})^*, \tag{11}$$

in which $(\cdot)^*$ denotes the complex conjugate. The equivalent of diagonal removal in conventional frequency domain beamforming can be accomplished by slightly modifying equation 11,

$$A_{j,k} = \frac{1}{2N(N-1)} \sum_{n=1}^{N} \sum_{\substack{m=1 \\ m \neq n}}^{N} \mathcal{F}_k(\tilde{\sigma}_{j,n}) \mathcal{F}_k(\tilde{\sigma}_{j,m})^*. \tag{12}$$

This alteration further improves the source map dynamic range, particularly when uncorrelated flow-noise is a contaminant in the measurement. To reduce random uncertainty in these spectral representations, blocks of data are ensemble-averaged according to Welch's method with a Hanning window and 75% overlap, resulting in a 10 Hz binwidth.

Uniform microphone weighting, as given above, will be compared to a coherence-based weighting scheme. This modifies equation 12 to be,

$$A_{j,k} = \frac{\displaystyle\sum_{n=1}^{N} \sum_{\substack{m=1 \\ m \neq n}}^{N} w_{k,n} w_{k,m} \mathcal{F}_k(\tilde{\sigma}_{j,n}) \mathcal{F}_k(\tilde{\sigma}_{j,m})^*}{\displaystyle 2 \sum_{n=1}^{N} \sum_{\substack{m=1 \\ m \neq n}}^{N} w_{k,n} w_{k,m}}. \tag{13}$$

There are many examples of microphone weighting schemes (for example, see Ref. 23). Selecting a simple scheme (Ref. 24) for initial assessment, the frequency dependent microphone weights can be defined as

$$w_{k,n} = \frac{1}{2} \lambda_n \left\{ 1 - \mathrm{Erf} \left[8 \left(\frac{r_n}{L_{\gamma,k}} - 1 \right) \right] \right\}. \tag{14}$$

The associated footprint of each individual microphone is accounted for by including λ_n. More specifically, λ_n^2 is the area (in m^2) allotted to each microphone based on the relative spacing of its neighbors. In other words, microphones toward the array center account for a small portion of the aperture and are scaled accordingly. The argument of the error function determines the effective aperture used at each frequency. Seeking to base this effective aperture on coherence, the ordinary magnitude-squared coherence is first computed between $N(N+1)/2$ microphone pairs over the flyover duration used for beamforming. Note that these signals were de-Dopplerized to follow the main rotor hub to avoid a reduction in coherence due to the Doppler effect. Coherence was then plotted as a function of the relative spacing of the microphone pairs. Examples of the coherence decay for the 20 kt flyover at 60 m AGL is given in Fig. 5(a) for 200 Hz and Fig. 5(b) for 2 kHz. Inspired by Ref. 25, a Gaussian curve was then fit to this decay, taking the form

$$\gamma_k^2 = \exp\left(- \left(\frac{\Delta r_{m,n}}{L_{\gamma,k}} \right)^2 \right). \tag{15}$$

Only data that resulted in $\gamma^2 > 0.2$ (unused data shown in red) was utilized to avoid misfitting. A coherence length scale, L_γ, is determined from the Gaussian fit and is shown in Fig. 5(c) for both altitude cases that will be discussed in the next section. These length scales are approximately inversely proportional to frequency, and used in equation 14.

Spatial integration of the source maps is useful to compare levels of individual noise sources. Using ROSI does not impose any restrictions on implementing how this is typically performed for conventional frequency domain beamforming. To obtain accurate levels, the integrated source levels are normalized by the integrated point spread function (PSF) located in the center of the integration region. Mathematically,

$$P = P_s \sum_{h=1}^{H} A_h \sum_{h=1}^{H} A_{s,h}^{-1} \tag{16}$$

in which P is the scan grid integrated source power, $A_{s,h}$ is the simulated PSF source power at scan grid location h within the user-defined integration region, and P_s is the total acoustic power of the PSF within the integration region. Figure 6 provides an example of the PSFs used when the aircraft is flying at 60 m AGL. For the lower-altitude flyover at 30 m AGL, these PSFs correspond to the array response at half of the denoted frequencies since resolution is inversely proportional to the distance between the phased array and the scan grid. For this initial effort, it is assumed that the PSFs are shift-invariant. In reality, the PSFs will be distorted when the aircraft is not

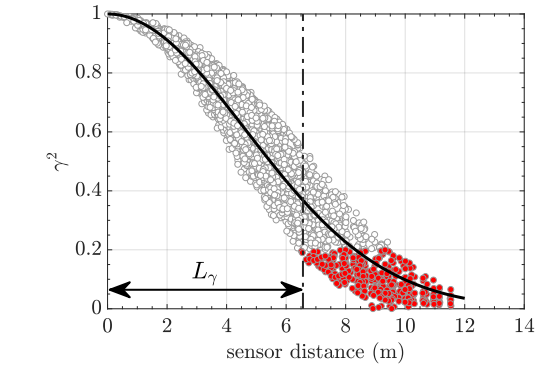

(a)

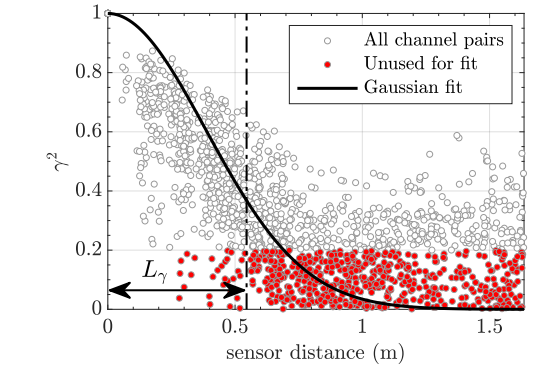

(b)

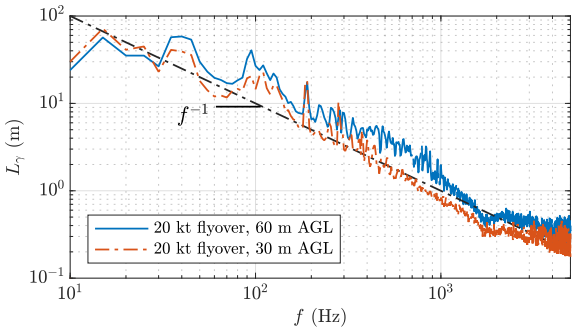

(c)

Figure 5. Coherence decay with relative spacing between microphones at (a) 200 Hz, (b) 2 kHz, and (c) the resulting frequency-dependent coherence length scale determined using a Gaussian fit (equation 15).

located directly above the array center. Future work will make an effort to account for this effect.

RESULTS

Source Localization

Source maps can be invaluable in understanding the dominant contributors to the overall acoustic field. For a helicopter such as the one used in these tests, it is common knowledge that the main rotor is often the dominant contributor. However, the tail rotor, engine noise, and the drivetrain are also sources that can produce nondeterministic noise, making it unclear if the ground measurements are purely the result of aeroacoustic sources produced by the main rotor, or a combination of the various components. In fact, the authors are not aware of any previous work that separates or isolates broadband contributions of the main rotor from flight test data. As previously mentioned, the fact that the scan grid rotates along with the main rotor effectively acts as a filter to other stationary sources, or sources rotating at different rates or in different planes.

The resulting source maps are provided in Figure 7 by applying the ROSI algorithm first to the 20 kt flyover at 60 m AGL. The focus will be on frequencies between 500 Hz and 4 kHz since this is the typical full-scale frequency range of nondeterministic sources for this type of aircraft. Several 1/3-octave bands are given. Only the 72-channel outer microphone array is used in this example, because ignoring the inner array enabled the highest dynamic range and greatest spatial resolution under uniform weighting (equation 12) for source localization. Still, poor resolution is found at 500 Hz, which is also the case for lower frequencies. Sources at the blade tips begin to be clear at 1 kHz, and obviously dominate at 2 and 4 kHz. Note the difference in dynamic range applied to the source maps at different frequencies – these ranges will be consistent for each frequency in additional figures that follow.

Figure 8 is the same flight condition, i.e., a 20 kt level flyover, but now flown at half the altitude as the previous case (30 m) above the phased array. Again, only the outer array is utilized here. A prominent feature of these source maps is the enhanced depiction of the sources located near the blade tips, specifically at the lower frequencies, and enough resolution to discriminate between blades. Note that because only information about the rotation *rate* was used (as opposed to azimuthal *position*) to process these data, the resulting source maps form hotspots at arbitrary azimuthal angles, although their relative spacing is consistent with the number of blades (360/5=72°). Thus, the source maps are rotated to coincide with the main rotor blades as depicted by the image of the helicopter. To this end, the exact source positions relative to the blades should not be scrutinized; rather, source positions should be accepted as qualitative. Additionally, blade sources represent azimuthal-averaged levels. In other words, these results do not indicate any differences associated with the advancing versus retreating sides. Ideally, all blades should result in similar levels, which is often the case here. Small discrepancies can be found and are likely the result of aircraft or main rotor position uncertainty or slight differences in the blades themselves.

One peculiar difference between the source maps at 60 m AGL case is the lack of noise identified at the hub axis at 30 m AGL. Aside from that, the blade noise sources are again localized towards the tips of the blades, as expected. Unfortunately, the 4 kHz source map illustrates no real identification of blade sources, but rather a collection of false sources toward the boundary of the scan grid. One potential reason for this difference could be directivity effects reducing the signal

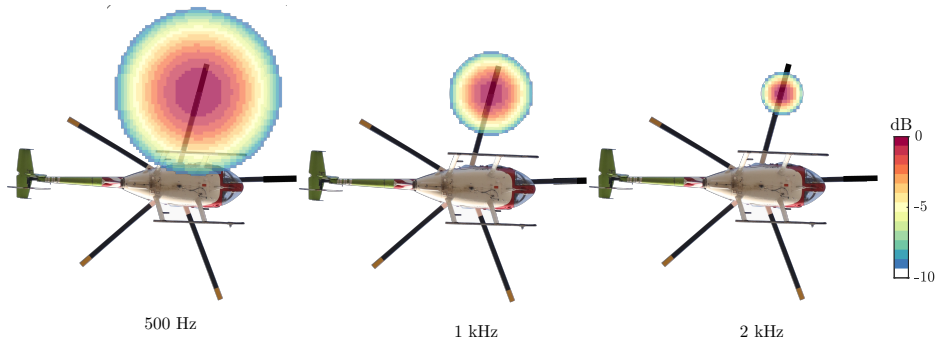

Figure 6. Sample point spread functions at three frequencies and a working distance of 60 m.

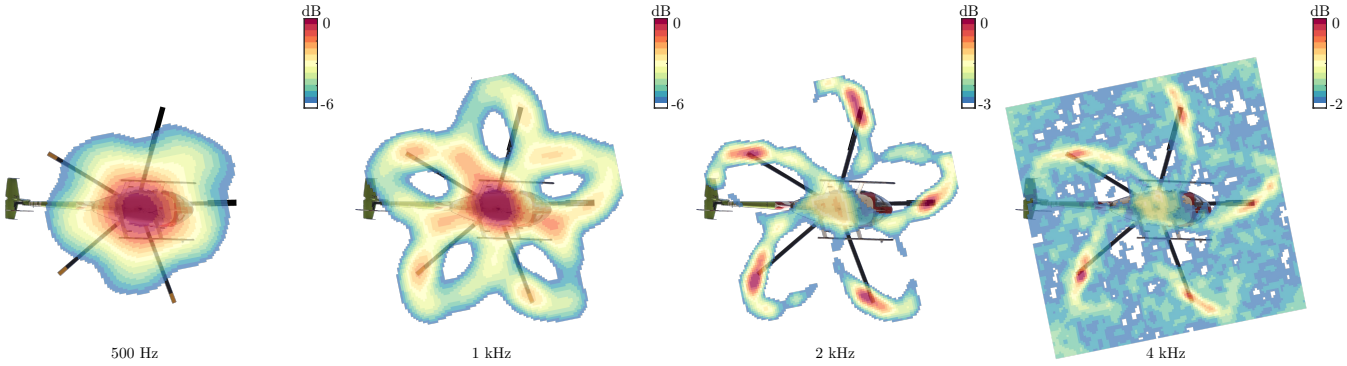

Figure 7. Source maps at various 1/3-octave frequencies for the 20 kt flyover at 60 m AGL, using only the outer array with uniform weighting.

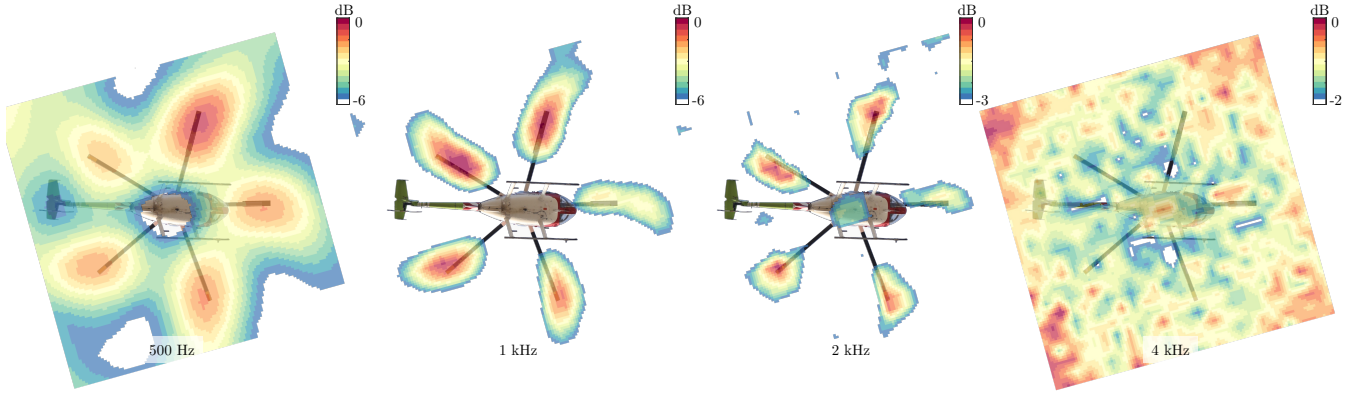

Figure 8. Source maps at various 1/3-octave frequencies for the 20 kt flyover at 30 m AGL, using only the outer array with uniform weighting.

coherence over the array. The coherence length scale is indeed smaller for this case for most frequencies (see Fig. 5(c)), albeit only slightly. When the helicopter is directly over the phased array, the array is covering approximately 22° of elevation at the lower altitude, but only covering approximately 11° for the higher altitude. Directivity features tend to get sharper with frequency, making this speculation plausible.

To combat this and enhance the identification of high-frequency sources, the coherence-based weighting scheme discussed earlier can be applied to de-emphasize or fully remove uncorrelated signals. Figure 9 does just that by applying equation 13 with the weighting given by equation 14 using all microphones (the outer and inner array together). Localization of the sources at 4 kHz is found to be much improved. At lower frequencies, the resolution is found to be degraded, but this effect is expected due to the lower weighting of the outer microphones, which drive overall spatial resolution.

Due to the enhanced source resolution at lower frequencies that the lower altitude provides, along with the ability of the coherence-based weighting scheme to clean up the source

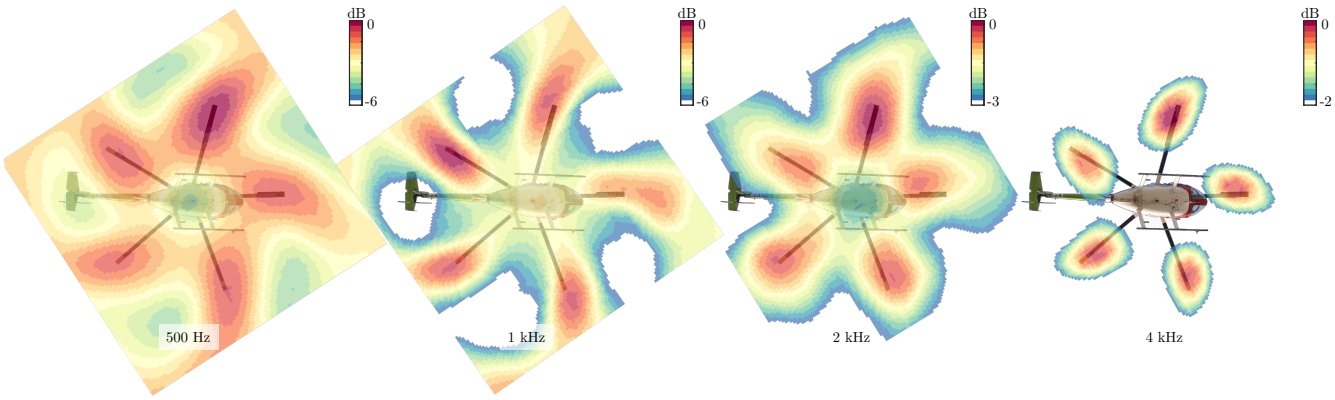

Figure 9. Source maps at various 1/3-octave frequencies for the 20 kt flyover at 30 m AGL, using all microphones with coherence-based weighting.

maps at higher frequencies, the recommendation for future testing would be to fly all test points at 30 m, if possible, when using a similar phased array layout. It is very likely, particularly with prototype or experimental aircraft, that a higher altitude would be required to ensure safety. If that is the case, the suggestion would be to increase the array's aperture while maintaining the same elevation angle coverage ($\approx 20°$). However, increasing aperture will necessitate an increase in channel count to avoid spatial aliasing and introducing false sources (e.g., decrease signal-to-noise) in the source maps.

Source Power Integration

Following suit of implementing a technique often leveraged for conventional frequency domain beamforming, levels can be integrated over regions of the source maps to compare relative strengths of the various components (via equation 16). Given only sources associated with the main rotor rotation are available due to the scan grid tracking, regions are selected that follow each of the five blades, depicted in Figure 10 as $\mathcal{I}_1$-$\mathcal{I}_5$. An additional region aligned with the hub axis, $\mathcal{I}_h$, is also defined to account for sources pertaining to the drivetrain or main rotor shaft. Both altitude cases are assessed with coherence-based weighting applied. Levels are all scaled to a 60 m reference distance. In the following discussion, a number of caveats are provided to acknowledge potential impacts of source level estimation that have yet to be fully investigated. Follow-on work focusing on limitations and assessing accuracy would prove useful to reduce the number of open questions.

Figure 11 provides the spectra of the 60 m AGL case for the hub, average levels over the five blades, total integrated levels over the 6 m by 6 m scan grid, and a representative de-Dopplerized single microphone. The single-microphone spectrum was computed similar to the beamforming results, i.e., using Welch's method with the same processing parameters. Although, the de-Dopplerization process was set to follow the

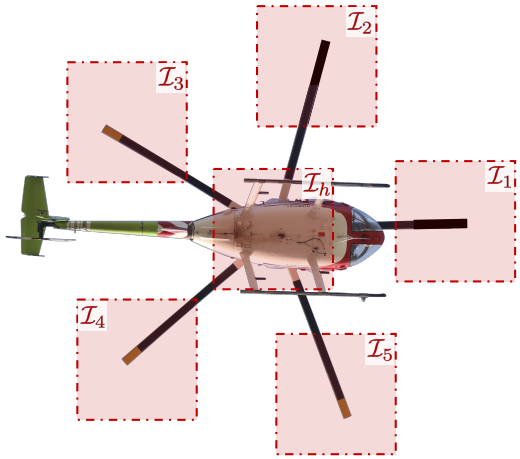

Figure 10. Definition of integration regions.

main rotor hub and so not accounting for rotation. Thus, rotational harmonic content of the main rotor may still be present in addition to the tonal content of the tail rotor and any other source on the aircraft. In contrast, the beamforming spectra do not demonstrate any sharp tonal features because the effect of rotation relative to the microphones has been removed. Note that while only the average beamformed individual blade noise is provided, the spectra of each blade were very similar and were within 2 dB of each other at all frequencies. At low frequencies (approaching 100 Hz), resolution is poor and results in a hotspot centered on the vehicle and region $\mathcal{I}_h$, causing the spectral levels of $\mathcal{I}_h$ to converge to integrated levels over the full source map. At mid-frequencies ($\approx$300 Hz to 1 kHz), the noise found at the hub is either equivalent to or greater than individual blade contributions. It is suspected that resolution is also lacking in this frequency range, causing energy to be focused toward the center of rotation (similar to the characteristics of the source map at 500 Hz in Figure 7).

The accuracy of the total integrated levels over the source map should be less sensitive to resolution. Comparing to the single-

microphone spectrum, total levels are approximately 10 dB down. This reason for this difference is unclear but could be due to other sources on the aircraft (e.g., the tail or engine) dominating in this frequency range. Alternatively, the beamforming process could be affected by coherence loss (even after applying coherence-based microphone weighting), uncertainties in the time-varying geometry used in the reception to source signal transformation, or that the sources are somewhat distributed and diverge from the assumption of point sources. Additional work would be needed to clarify this. Beyond 2 kHz, however, the total integrated levels of the rotating scan plan converge onto the single microphone spectrum, suggesting blade noise dominates this part of overall aircraft levels.

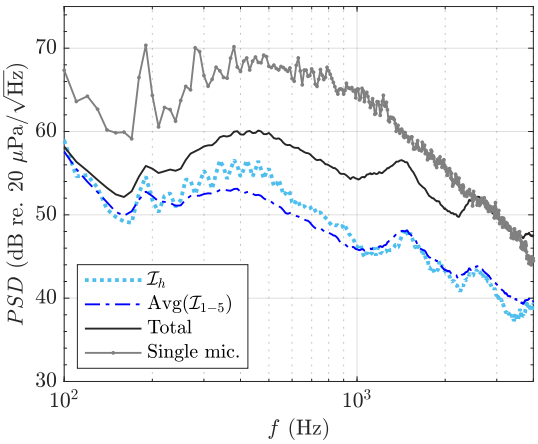

Figure 11. Integrated spectra displaying relative contributions between the noise found at the hub, the average value of the individual blades, and total integrated level over the scan grid for the 20 kt flyover at 60 m AGL.

Figure 12 gives the integrated spectra from the same scan grid regions for the 30 m AGL case. Here, the individual blade contributions are higher than levels found in the hub region for nearly all frequencies. This trend is consistent with the corresponding source maps in Figure 9. The discrepancy in the two altitude cases between relative levels of the blades and the hub region further suggests this being an effect of the beamforming process, and in particular, inadequate resolution. Advanced beamforming techniques would be beneficial and likely improve the relative source ranking. That said, the lower-altitude condition is preferred independent of processing technique. In any case, similar trends are found between the integrated and single-microphone levels, with the largest difference again found at the mid frequencies.

The single-microphone and total integrated spectra from Figures 11 and 12 are plotted in Figure 13 for comparison. Despite slight differences in levels, the single-microphone spectrum of the 60 m AGL flyover is strikingly similar to what was measured for 30 m AGL, indicating good repeatability of the test conditions. Note that levels were scaled to 60 m AGL and compensated for atmospheric attenuation (although the latter was a negligible effect). It would then be expected that the

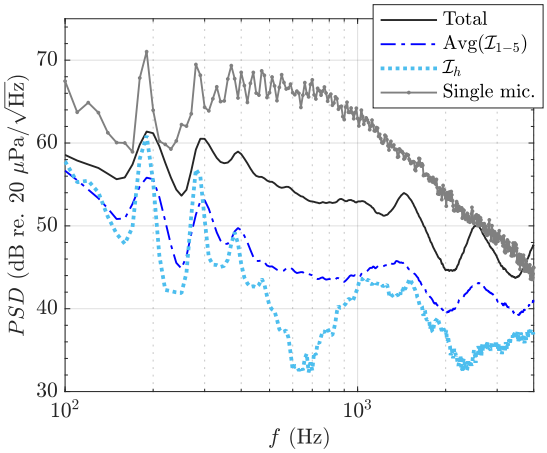

Figure 12. Integrated spectra displaying relative contributions between the noise found at the hub, the average value of the individual blades, and total integrated level over the scan grid for the 20 kt flyover at 30 m AGL.

integrated spectra from ROSI would be consistent for the two flyovers. In a rough sense, levels are indeed similar, but differences in excess of 5 dB exist. The duration of the flyover, and hence number of main rotor revolutions (≈40), is limited. Thus, a higher number of flyovers may be needed at the same condition to reduce uncertainty, with this requirement increasing in necessity if forward flight speed is increased.

One interesting consistency is the presence of spectral hump features at approximately 1.5 and 2.5 kHz that would otherwise not be seen without the assistance of a phased array. These features are also in the individual blade spectra, so these may be tied to self-noise type sources.

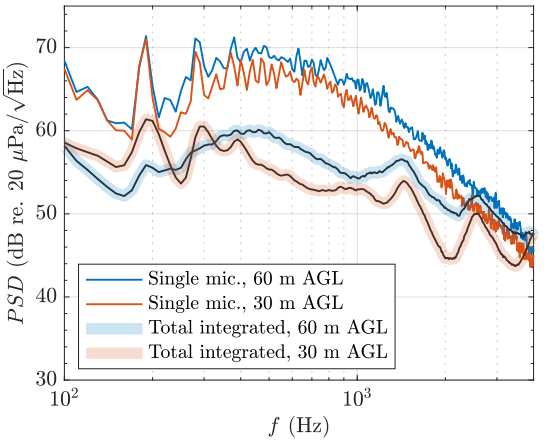

Figure 13. Autospectral density of raw single microphone signals and total source map integrated levels for flyovers at both altitudes.

CONCLUDING REMARKS

The ROtating Source Identifier (ROSI) time-domain beamforming algorithm was implemented to assess its feasibility of

gaining greater physical insight from acoustic measurements of rotating sources in forward flight. A 20 kt case was used for this initial effort and applied to data acquired during flyovers at both 60 and 30 m above a 117-channel ground-based phased array.

Source maps showed good localization of aeroacoustic sources near the blade tips over a range of frequencies, i.e., 1/3-octave bands from 500 Hz to 4 kHz, with the best results provided at the lower altitude with the coherence-based weighting scheme applied. A general recommendation can be made for future testing to maintain a similar ratio of array aperture to the lower tested flight altitude (i.e., the elevation viewing angle range, approximately 20°) for similar characteristic length scales of the helicopter tested here. However, a higher channel count may be needed for analysis at higher flight altitudes.

As shown herein, tail rotor noise was effectively filtered out through the use of a scan grid rotating in the plane of the main rotor at its rotation rate. If the array layout is properly planned, source ranking can be at least qualitatively achieved for aircraft with multiple rotating propulsors. Such information will be pertinent to guide research for vehicles where little is known about their overall acoustic characteristics (i.e., UAM, FVL aircraft).

Integrated spectra were computed to estimate the noise generated by the blades and noise found near the center of rotation. In a rough sense, levels from the two flyovers agree, although differences in excess of 5 dB were found. Multiple flyovers at the same condition would be useful to study repeatability and the uncertainty in beamforming processing, particularly because the duration of the event is limited by forward flight. This necessity will be of increasing importance when investigating higher forward flight speeds.

Total integrated levels are approximately 10 dB lower at mid-frequencies as compared to a single microphone. Additional analysis is needed to understand if this is an underestimation of the main rotor source noise, or if other components on the aircraft are larger contributors. In any case, this method shows promise in source separation to better understand full-vehicle noise characteristics through identification of its relative contributors, progressing toward an improved comparison dataset for validation of prediction tools.

ACKNOWLEDGMENTS

The authors would like to thank the team for their outstanding dedication and hard work that made this test possible. US Army: Dr. Oliver Wong, Dr. Shawn Naigle, Tom Maier, and Jacob Wilson. NASA Langley: Alonzo 'Max' Reid, Benny Lunsford, Dr. Noah Schiller, and Dr. Michael Doty. Sierra Army Depot: Margarita Gonzalez Venegas, Michael Foley, and Michael Gray. Helicopter Technology Company: Jack Rajcic, Jay Wigginton (Pilot), Charles Dean (Chief Engineer), Gary Budorf, and Brian Cicerone. The authors would especially like to thank the efforts of the contractors who supported the equipment development and data acquisition efforts, including Jeffrey Davis and David Ridgway of Analytical Mechanics Associates and Stanley Mason from Jacobs Technology, Inc. Finally, we appreciate the technical insights provided by Dr. Nikolas Zawodny from NASA Langley.

REFERENCES

1. Hubbard, H., "Aeroacoustics of Flight Vehicles: Theory and Practice. Volume 1: Noise Sources," NASA RP 1258, 1991.

2. Greenwood, E., and Schmitz, F., "Separation of main and tail rotor noise from ground-based acoustic measurements," *Journal of Aircraft*, Vol. 51, (2), 2014, pp. 464–472.

3. Stephenson, J., and Tinney, C., "Extracting blade–vortex interactions using continuous wavelet transforms," *Journal of the American Helicopter Society*, Vol. 62, (2), 2017, pp. 1–10.

4. Rachaprolu, J., and Greenwood, E., "Helicopter noise source separation using an order tracking filter," *Journal of the American Helicopter Society*, Vol. 69, (1), 2024, pp. 1–9.

5. Rachaprolu, J., Valente, V., ElSharkawy, E., and Greenwood, E., "Multirotor Noise Source Separation and Characterization from Ground-Based Acoustic Measurements," Proceedings of the 80th Annual Forum of the Vertical Flight Society, 2024.

6. Pascioni, K., Thai, A., and Bain, J., "Propeller Source Noise Separation from Flight Test Measurements of the Joby Aviation Aircraft," 30th AIAA/CEAS Aeroacoustics Conference, AIAA Paper 2024-3231, 2024.

7. Stephenson, J., Pascioni, K., Houston, M., Stutz, C., and Martin, P., "Overview of a Comprehensive MD530F Acoustic Flight Test," Proceedings of the 81st Annual Forum of the Vertical Flight Society, 2025.

8. Houston, M., Stephenson, J., Pascioni, K., and Stutz, C., "Snapshot Array Design Considerations for Rotorcraft Noise Characterization," Proceedings of the 81st Annual Forum of the Vertical Flight Society, 2025.

9. Greenwood, E., Brentner, K., Rau, R., and Gan, Z., "Challenges and opportunities for low noise electric aircraft," *International Journal of Aeroacoustics*, Vol. 21, (5-7), 2022, pp. 315–381.

10. Merino-Martínez, R., Snellen, M., and Simons, D., "Functional beamforming applied to imaging of flyover noise on landing aircraft," *Journal of Aircraft*, Vol. 53, (6), 2016, pp. 1830–1843.

11. Khorrami, M., Lockard, D., Humphreys, W., and Ravetta, P., "Flight-Test Evaluation of Airframe Noise Mitigation Technologies," 2018 AIAA/CEAS Aeroacoustics Conference, AIAA Paper 2018-2972, 2018.

12. Humphreys, W., Lockard, D., Khorrami, M., Culliton, W., McSwain, R., Dolph, C., and Ravetta, P., "Development of a Field-Deployable Microphone Phased Array for Airframe Noise Flyover Measurements," NASA TM 2023-0010620, 2023.

13. Sijtsma, P., Oerlemans, S., and Holthusen, H., "Location of Rotating Sources by Phased Array Measurements," 7th AIAA/CEAS Aeroacoustics Conference, AIAA Paper 2001-2167, 2001.

14. Yu, L., Wu, H., Antoni, J., and Jiang, W., "Extraction and imaging of aerodynamically generated sound field of rotor blades in the wind tunnel test," *Mechanical Systems and Signal Processing*, Vol. 116, 2019, pp. 1017–1028.

15. Wang, R., Jing, Q., Yu, L., Zhang, Y., and Yu, L., "The acoustic imaging of the broadband dipole sound sources of helicopter rotor in the wind tunnel test," *IEEE Transactions on Instrumentation and Measurement*, Vol. 71, 2022, pp. 1–11.

16. von den Hoff, B., Simons, D., and Snellen, M., "Breakdown of Propeller Aircraft Noise by Applying Conventional Beamforming Jointly with Imaging Using the Rotating Source Identifier," 9th Berlin Beamforming Conference, BeBeC-2022-D02, 2022.

17. Chen, W., and Huang, X., "Wavelet-based beamforming for high-speed rotating acoustic source," *IEEE Access*, Vol. 6, 2018, pp. 10231–10239.

18. Jingyu, H., Baohong, B., Yingzhe, Z., Dakai, L., and Wenxin, L., "Wavelet-based Functional Beamforming Method for Aeroacoustics Moving Sources Localization," 4th International Conference on Information Communication and Signal Processing (ICICSP), 2021.

19. Pascioni, K., Greenwood, E., Watts, M., Smith, C., and Stephenson, J., "Medium-Sized Helicopter Noise Abatement Flight Test Data Report," NASA TM 2021-0011459, 2021.

20. Stephenson, J., Lind, A., Hutchins, C., Pascioni, K., Houston, M., and Martin, P., "Yuma 2022 Rotorcraft Acoustic Flight Test," NASA TM 2022-0004483, 2022.

21. Schmitz, F., "Reduction of Blade-Vortex Interaction (BVI) Noise through X-Force Control," *Journal of the American Helicopter Society*, Vol. 43, (1), 1998, pp. 14–24.

22. Greenwood, E., Sim, B., and Boyd, D., "Effects of Ambient Conditions on Helicopter Harmonic Noise Radiation: Theory and Experiment," *Journal of the American Helicopter Society*, Vol. 69, (1), 2024, pp. 1–17.

23. Bahr, C., and Lockard, D., "Designing Shading Schemes for Microphone Phased Arrays," 8th Berlin Beamforming Conference, BeBeC-2020-S1, 2020.

24. Sijtsma, P., and Stoker, R., "Determination of Absolute Contributions of Aircraft Noise Components using Fly-Over Array Measurements," 10th AIAA/CEAS aeroacoustics conference, AIAA Paper 2004-2958, 2004.

25. Lockard, D., and Choudhari, M., "Noise Radiation from a Leading-Edge Slat," 15th AIAA/CEAS Aeroacoustics Conference (30th AIAA Aeroacoustics Conference), AIAA Paper 2009-3101, 2009.